A 7-mg miniature catalytic-combustion engine for millimeter-scale robotic actuation

Fares Maimani, Ariel A. Calderón, Xiufeng Yang, Alberto Rigo, Joey Z. Ge, Néstor O. Pérez-Arancibia *

Department of Aerospace and Mechanical Engineering, University of Southern California (USC), Los Angeles, CA 90089-1453, USA

ABSTRACT

Microrobots at the subcentimeter scale have the potential to perform useful complex tasks if they were to become energy independent and could operate autonomously. The vast majority of current microrobotic systems lack the ability to carry sufficient onboard power to operate and, therefore, remain tethered to stationary sources of energy in laboratory environments. Recent published work demonstrated that chemical fuels can react under feedback control on the surfaces of tensioned *shape-memory alloy* (SMA) *nickel-titanium* (NiTi) wires coated with *platinum* (Pt) catalyst. Combining catalytic combustion of fuels with high energy densities with the high work densities of SMA wires is a promising approach to provide onboard power to microrobots. In this article, we present a novel 7-mg SMA-based miniature catalytic-combustion engine for millimeter-scale robotic actuation that is composed of a looped NiTi-Pt composite wire with a core diameter of 38 μm and a flat carbon-fiber beam with a length of 13 mm. This beam acts as a leaf spring during operation. The proposed design of the engine has a flat and narrow geometry, functions according to a periodic-unimorph actuation mode, and can operate at frequencies as high as 6 Hz and lift 650 times its own weight while functioning at 1 Hz, thus producing 39.5 μW of average power in the process. For the purposes of design and analysis, we derived a model of the heat transfer processes involved during actuation, which combined with a Preisach-model-based description of the SMA wire dynamics, enabled us to numerically simulate the response of the miniature system, and thus predict its performance in terms of frequency and actuation output. The suitability for microrobotics and functionality of the proposed approach is demonstrated through experimental results using a custom-built fast-response high-precision system of fuel delivery.

1. Introduction

Fully autonomous microrobots at the subcentimeter scale will revolutionize many fields such as surveillance, drug-delivery, search and rescue, and artificial pollination. However, due to a lack of adequate power systems that can operate the robots in a tetherless and autonomous way, most microrobots are usually only operable inside labs where they are connected to stationary power systems. Fully autonomous microrobots must be able to operate and achieve a goal without depending on any external system [1]. We define untethered microrobots as robots that can operate without being connected through cables to any external system. Untethered microrobots may connect wirelessly to external systems for power or control. In this article, we use the term microrobot to describe miniaturized robots with characteristic

lengths at the subcentimeter scale. To achieve untethered operation, microrobots need power systems that can be added on board, or external power systems that can deliver power wirelessly. In the case of onboard power, the system needs to have adequate specific energy and specific power ratings to supply the microrobot with the energy required for its operation. In this article, we demonstrate combining catalytic combustion of fuels with high energy densities with the high work densities of shape-memory allow wires as an approach to provide onboard power to microrobots (Fig. 1). The traditional technologies and approaches used in the literature cannot easily meet the requirements for powering autonomous microrobots.

Wireless external power sources have been investigated to different levels of success to build untethered microrobots. Different research groups have used lasers [2], solar power [3], vibration fields [4], and magnetic fields [5,6] to power and control microrobots. While

Nomenclature

A	contact area (m^2)
A_{SMA}	cross-sectional area of SMA wire (m^2)
b	offset distance between SMA and neutral axis (m)
B_i	Biot number (–)
β	heat transfer correction factor (–)
C_P	specific heat capacity (J K^{-1} kg^{-1})
d	displacement (m)
E	total energy (J)
EI	bending stiffness (M m^2)
ϵ	Cauchy normal strain (–)
$\dot{f}$	mass flow rate (kg s^{-1})
F	force (N)
g	gravity acceleration (m s^{-2})
$\bar{h}$	average heat transfer coefficient (W m^{-2} K^{-1})

|	
ΔH_{rxn}	specific heat of reaction (J kg^{-1})
k	thermal conductivity (W m^{-1} K^{-1})
L	length (m)
L_{cond}	length of conduction path (m)
m	mass (kg)
P	normal force (N)
$\dot{Q}_{x \to y}$	energy transfer rate from x to y (J s^{-1})
r	radius (m)
SCCM	standard cubic centimeters per minute (cm^3 min^{-1})
σ	normal stress (N m^{-2})
T	temperature (K)
U_{x-y}	overall heat transfer coefficient between x and y (W m^{-2} K^{-1})
w	actuator tip linear displacement (m)
W	work output (J)
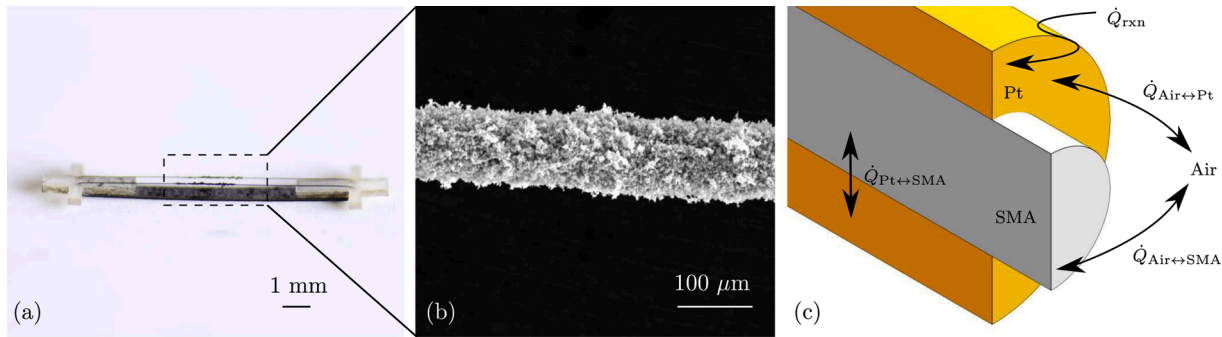
Fig. 1. The miniature catalytic-combustion engine. (a) Close-up picture of the miniature engine. Shown in the dashed rectangle is the coated portion of the SMA wire. (b) SEM image of the Pt coating layer on an SMA wire. The catalytic coating layer is rough and porous and has a thickness of 18 μm. (c) Conceptual schematic that shows the allowed energy exchange paths in the thermal model of the SMA-Pt system.
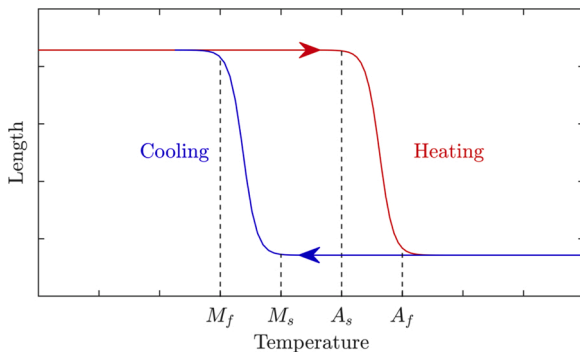

Fig. 2. Typical hysteresis transformation curve for an SMA wire under constant stress during heating and cooling. A_s: austenite start, A_f: austenite finish, M_s: martensite start, M_f: martensite finish.

promising, wireless power sources do not allow for full autonomy, and, as a result, they limit the scope of the environment in which microrobots can operate in while also limiting their the versatility and robustness. Furthermore, powering and controlling multiple microrobots independently through wireless power fields is challenging. To design a robust and versatile microrobot, we believe that a power source with high specific energy and specific power must be carried on board the microrobot.

The majority of microrobots with onboard power architectures proposed in the literature utilizes actuation systems that converts electrical energy to mechanical energy in order to locomote. The main technologies used in those designs are piezoelectric effect [7,8], electrostatic actuators [9], and shape-memory alloys (SMAs) [10,11]. Piezoelectric actuation systems are robust and operate at high frequencies, but they require high voltage electronics [12]. Electrostatic actuators are energy efficient and can operate at high frequencies, but they also suffer from low energy densities and need high voltages [12]. SMAs are smart materials, usually made of nickel-titanium (NiTi), that have crystal structures and can strain in response to temperature and stress changes. Tensioned SMA wires contract when heated and recover their original shape when cooled down while exhibiting a shape-memory effect [13] (Fig. 2). SMA-based actuators have high power densities and require relatively low voltages, but their operation bandwidth is limited by the time required for cooling the SMA back to its original shape [14].

One approach to provide electrical input to microrobotic actuation systems is to use onboard batteries. State of the art battery technology cannot easily power microrobots because of their limited specific energy and specific power ratings. Batteries have been successfully used in autonomous robots with length scales as small as 4 cm [15]. However, for smaller robots at the subcentimeter scale, using batteries is difficult because of the relative large battery mass and the required components to interface between the battery and the actuation mechanism. For example, the SMALLBug shown in Ref. [16] is a 1.2 cm, 30 mg crawling microrobot that uses an SMA actuator and requires 135 mW of average power to operate at a frequency and speed of 20 Hz and 17 mm s^{-1},
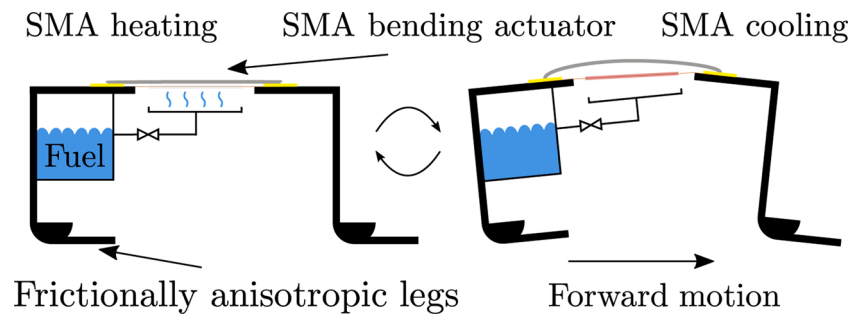
Fig. 3. Conceptual design of a robot utilizing the miniature catalytic-combustion engine for actuation. A Fuel tank releases fuel periodically to react with the catalytic layer coating the SMA wire. The actuator body provides preloads the SMA wire. The heat of reaction and the preload stress causes the SMA wire to contract and recover its shape cyclically. Frictional anisotropic legs converts the cyclic strain deformation of the SMA to forward motion of the robot.

respectively. To operate the SMALLBug for 10 min using state of the art Li-ion batteries with a specific energy and specific power of 0.875 MJ kg^{-1} and 340 W kg^{-1}, respectively, the required battery will weigh 400 mg, or 13 times the robot weight [17]. Additional weight is further required to meet the instantaneous power requirements of the SMALLBug, to interface between the battery and the actuation system, and to power any additional onboard systems. This calculation also assumes that batteries' specific energy and specific power do not decrease at small scales. Beside batteries, other novel approaches such as using living cells on board to power and actuate microrobots have also been investigated [18].

A more promising approach toward having onboard power in microrobots is to use chemical fuels, such as hydrogen or hydrocarbons, as an alternative to batteries. This approach is more promising because chemical fuels have high specific energy (45 MJ kg^{-1} for butane) and high specific power when combined with an appropriate heat engine. Miniaturizing a traditional heat engine is difficult because of fabrication challenges and efficiency reductions due to friction and heat losses. One concept that has been investigated is to design miniature heat engines using SMAs. The shape-memory effect of SMA wires allows them to be used in an analogous way to working fluids in heat engines to convert chemical energy to mechanical work.

Early work investigated using SMA coils to build large heat engines [19], but most efforts failed due to scaling issues. More recently, SMA engines and actuators have been built successfully at smaller scales in many fields such as robotics [20,21], MEMS [22], wireless sensors [23], and microfluidics [24].

The majority of SMA actuators use electricity to heat up the SMA through Joule heating and use ambient air for cooling. The majority of SMA heat engines use a stationary hot source, such as hot water, to heat up the SMA. Those designs do not address how the hot source can be powered at the relevant scale. A promising approach to heat up the SMA has been to use platinum (Pt) catalyst to perform catalytic combustion of chemical fuels on or near the SMA. Early attempts demonstrated the concept but only succeeded at achieving slow actuation frequencies (<0.1 Hz) [25,26]. Other efforts investigated catalytically burning liquid propellant fuels to actuate microrobots by utilizing the hot product gases of combustion [27]. Recent work successfully demonstrated that SMA wires coated with Pt can dependably actuate microrobots using hydrogen, methanol, or butane with frequencies up to 1 Hz [20,28]. Our lab successfully demonstrated the RoBeetle, an autonomous 1.5 cm microrobotic crawler that catalytically burns methanol on a Pt-coated SMA wire to move with speeds up to 0.76 mm s^{-1} [20].

In this work, we continue the previous efforts done in our lab to develop high frequency microrobotic SMA actuation systems. Inspired by the fast actuation technology of the SMALLBug and the catalytic combustion innovations of the RoBeetle, we propose a novel 7 mg miniature catalytic-combustion engine for millimeter-scale robotic actuation and demonstrate its operation with frequencies up to 6 Hz (Fig. 1a). For the rest of the paper, we use the words *engine* and *actuator*

interchangeably to describe the proposed SMA-based device, which converts chemical energy to mechanical work.

To design our miniature catalytic-combustion engine, we started from the actuator presented in Ref. [16] and modified it to be powered by hydrogen fuel. We performed thermal and dynamic analysis on the miniature engine to demonstrate the design validity and model the engine's performance. To test the engine and its control strategy, we built an experimental characterization setup and an advanced fuel delivery system that can be used to characterize engines and design control strategies. The presented miniature engine demonstrates a path toward improving the design and increasing the frequency of SMA-based miniature catalytic-combustion engines that can potentially be used in autonomous microrobots.

The conceptual design illustrated in Fig. 3 demonstrates how the proposed miniature catalytic-combustion engine can be implemented in a microrobotic application. The proposed actuator and a fuel tank are attached to a robotic structure similar to the one presented in [16]. The tank is preprogrammed to releases fuel periodically. The fuel reacts on the catalytic surface causing the SMA wire temperature to oscillate. The actuator body acts as a spring to preload the SMA wire. The preload stress and the temperature oscillation causes the SMA wire to contract and expand repeatedly. The frictionally anisotropic legs of the robot convert the cyclic strain deformations of the SMA wire to a forward motion of the robot. The characterization setup we built can be used to test control and fuel delivery strategies. Then, the preprogrammed, onboard tank and valve system can deliver the fuel to the actuator in a way that achieves the desired functional and performative requirements of the microrobot.

The rest of the paper is organized as follows. First, we discuss the fabrication and design process of the novel miniature catalytic-combustion engines. Then, we present the thermal and dynamic analysis of the proposed miniature engine. After, we describe the characterization setup and the fuel delivery system and show results of operating the engine while performing work. Finally, we discuss conclusions and a path toward implementing the presented innovations in fully autonomous microrobots.

2. Design and fabrication

The design of the miniature engine utilizes a cantilever SMA bending actuator [29], where an SMA wire connects both ends of a cantilever beam. As the SMA wire is heated, it contracts due to the shape-memory effect and as a result the cantilever beam bends. Our engine consists of a carbon fiber beam with ends made of high temperature reinforced epoxy laminate (FR4). Each end contains two orifices. An SMA wire with a length approximately twice the beam's length is threaded through each orifice, forming a loop and connecting both FR4 ends. The FR4 is used to protect the epoxy present in the carbon fiber, which is not able to stand the high temperatures reached by the SMA wire during actuation. This configuration allows for the carbon-fiber beam to be used as a spring
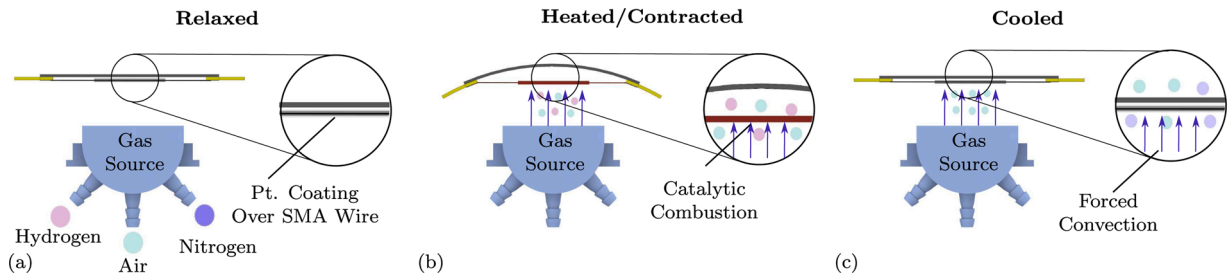
Fig. 4. Design of the miniature catalytic-combustion engine (a) A segment of SMA wires are coated with Pt. When no fuel is present to initiate catalytic combustion, the actuator stays in its relaxed position. (b) When a gas source introduces fuel gas around the Pt coating layer, catalytic combustion starts. The heat released from the reaction results in the shortening of the SMA wire, which creates bending motion on the actuator. (c) The gas source supplies an air flow to increase the cooling rate by convection. As a result, the actuator goes back to its relaxed position.
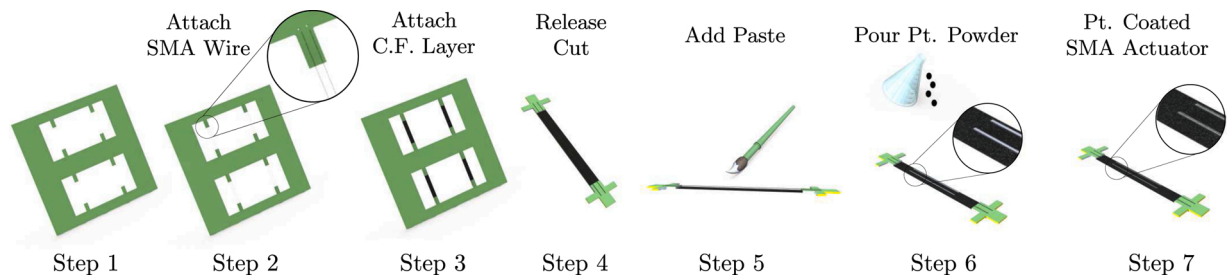

Fig. 5. Fabrication of the SMA based actuators. Step 1: A jig of FR4 is pre-cut using a high resolution laser cutter. Step 2: An SMA wire is looped in the orifices of the jig and secured at the ends using glue and knots. The SMA wire must be kept in tension. Step 3: Using the tabs in the jig, a carbon fiber layer is glued to the back of the jig. Step 4: The jig is aligned and cut using the high resolution laser cutter. Step 5: A thermally conductive paste is added to the surface of the SMA. A brush is used to manually add the paste evenly in a section of the wire. Step 6: Pt powder is poured over the actuator. The Pt powder coats the SMA surface area with where the paste was applied. Step 7: The actuator is ready to be used.

that holds the SMA wires in tension, while protecting the carbon fiber from the high temperatures of the wire.

The SMA wire is coated with Platinum black powder which creates a catalytic surface. When fuel comes in contact with the surface, a catalytic combustion reaction takes place on the Pt coating which increases the Pt layer temperature. As a result, the SMA wire heats up through conduction, activating the shape-memory effect and shortening its length. The geometric constraints transform the strain generated by the SMA into a bending of the central carbon fiber beam. When the fuel is not applied, the SMA cools down, and the restorative force of the carbon fiber brings the actuator to its original position. Fig 4 illustrates a diagram with the actuator states.

Two design innovations allow us to operate this actuator at frequencies higher than 1 Hz. First, the use of thin wires ($r = 19.05\,\mu m$) decreases the thermal mass, allowing for fast cooling and heating. The disadvantage of using thinner wires is that they produce smaller forces. We overcome this disadvantage by using two wires in parallel to increase the force generated while maintaining the fast heating and cooling. The second design innovation is the use of the central carbon fiber, which serves two purposes. It maintains the SMA wires in tension and it acts as a spring that helps the actuator restore its original shape when bent.

The fabrication relies on laser cutting, manual positioning, and gluing of elements as shown in Fig. 5. To cut the materials, we use a diode-pumped solid-state ultraviolet laser (Photonics Industries DCH-355-3) with a wavelength of 355 nm and a spot diameter of 10 μm. The process starts with a laminate of FR4 with a thickness of 127 μm. The laminate is cut into a geometry which is used as a jig to place the actuator's components during fabrication (Fig. 5-step 1). During the laser cut, orifices are engraved on the jig which are used to thread the SMA wires (Fig. 5-step 2). The SMA wire (FLEXINOL) is looped through the orifices and tied using a simple knot to maintain its tension and secure its position. The amount of tension is controlled visually. If the

wire is not fully extended, then the tension is insufficient. If the central carbon fiber bends due to the tension applied, then the SMA is in over-tension. To prevent unraveling and to hold the wire in place in the FR4 jig, a small amount of *cyanoacrylate* (CA) glue is applied carefully with a brush to the contact area between the SMA knot and the FR4.

The carbon fiber beam is fabricated from a stack using four layers of *Tenax* unidirectional prepreg carbon fiber. The fiber direction of the layers is set to [0° 90° 90° 0°] where the 0° direction aligns with the bending direction. The four layers are cured via a process of pressure and temperature to generate a final carbon stack that has a thickness of 90 μm. Rectangular beams are then cut from the stack using the laser system, with a length and width of 10 and 2 mm, respectively. After that, the carbon fiber beams are manually glued onto the back of the FR4 jig (Fig. 5-Step 3). Next, a release cut is performed to separate the assembled actuators from the jig (Fig. 5-step 4).

The catalytic surface over the SMA wire is obtained via a selective adhesion process. First, thermal paste (*Omegatherm 201*, OMEGA) is applied to the SMA in tension via a brush creating an area on the wire with adhesion (Fig. 5-Step 5). We applied the thermal paste to create a homogeneous coating layer that covers roughly half of the SMA wire. Then, Pt powder is poured over the actuator (Fig. 5-Step 6), fully covering the SMA wire. The powder gets selectively attached to the area of the SMA wire where the paste was applied, producing a coating surface ready for catalytic combustion (Fig. 5-Step 7).

3. Engine model

We analyzed the thermal and dynamic behavior of the engine to validate the design and predict the maximum possible frequency and displacement. A lumped capacitance heat transfer model was used to estimate the SMA temperature during operation. The model examines an SMA wire actuator coated with a Pt powder layer. Fig. 1 shows the actual miniature catalytic-combustion engine system, while Fig. 1c displays the

Table 1
Biot Number for the radial and longitudinal dimensions in the system.

System and dimension	B_i
SMA radial	7.2×10^{-4}
SMA longitudinal	0.38
Pt radial	1.6×10^{-4}
Pt longitudinal	0.21

conceptual setup of the thermal model. In this theoretical analysis, the SMA wire and the coating layer are treated as two concentric cylinders. The lumped capacitance assumption was used because the Biot numbers (B_i) for the SMA wire and the coating layer were less than unity. The Biot number was calculated using the definition in Eq. (1) adopted from Ref. [30]. The summary of the results are shown in Table 1:

$$B_i = \frac{L_{\text{cond}}\overline{h}}{k} \tag{1}$$

The lumped capacitance assumption allows us to perform temporal analysis while assuming uniform spatial temperature distribution. We assume that the SMA wire can exchange energy with the surrounding air and the coating layer, and the coating layer can exchange energy with the surrounding air and the SMA wire (Fig. 1c). Additionally, energy can be added directly to the coating layer by the heat of reaction source term $\dot{Q}_{\text{rxn}}$. By performing an energy balance on the SMA wire and on the coating layer, we obtain Eqs. (2) and (3):

$$\frac{dE_{\text{SMA}}}{dt} = \dot{Q}_{\text{Pt}\rightarrow\text{SMA}} + \dot{Q}_{\text{air}\rightarrow\text{SMA}} \tag{2}$$

$$\frac{dE_{\text{Pt}}}{dt} = -\dot{Q}_{\text{Pt}\rightarrow\text{SMA}} + \dot{Q}_{\text{air}\rightarrow\text{Pt}} + \dot{Q}_{\text{rxn}} \tag{3}$$

We assume constant properties of the system and constant ambient temperature ($T_{\text{amb}} = 298$ K) and relate $\dot{Q}_{\text{rxn}}$ directly to the fuel flow rate. Then we can derive Eqs. (4) and (5):

$$m_{\text{SMA}}C_{P_{\text{SMA}}}\frac{dT_{\text{SMA}}}{dt} = U_{\text{SMA}-\text{Pt}}A(T_{\text{Pt}} - T_{\text{SMA}}) + \overline{h}_{\text{air}-\text{SMA}}A(T_{\text{Amb}} - T_{\text{SMA}}) \tag{4}$$

$$m_{\text{Pt}}C_{P_{\text{Pt}}}\frac{dT_{\text{Pt}}}{dt} = -U_{\text{SMA}-\text{Pt}}A(T_{\text{Pt}} - T_{\text{SMA}}) + \overline{h}_{\text{air}-\text{Pt}}A(T_{\text{Amb}} - T_{\text{Pt}}) + \Delta H_{\text{rxn}}\dot{f}_{\text{H}_2} \tag{5}$$

The average heat transfer coefficients ($\overline{h}_{\text{air}-\text{SMA}}$ and $\overline{h}_{\text{air}-\text{Pt}}$) were calculated using Eq. (6) adopted from Ref. [30]. The value of r equals the radius of the SMA wire or the outer radius of the coating layer.

$$\overline{h} = \frac{k_{\text{air},25°\text{C}}}{2r} \tag{6}$$

The values of the heat transfer coefficient between the SMA wire and the coating layer ($U_{\text{SMA}-\text{Pt}}$) were calculated using Eq. (7) adopted from Ref. [30]. We added β as a correction factor that accounts for the contact imperfections between the SMA and the coating layer and accounts for the thermal resistance of the glue layer. In our analyses, we set $\beta = 4.9 \times 10^{-5}$. We found that this value of β provides better agreement with experimental results, since we observe experimentally that there are large differences between the temperatures of the SMA wire and the coating layer:

$$(UA)_{\text{SMA}-\text{Pt}} = \beta \left(\frac{ln\left(\frac{r_{\text{Pt}}}{r_{\text{SMA}}}\right)}{2\pi k_{\text{Pt}}L_{\text{Pt}}} + \frac{ln\left(\frac{r_{\text{SMA}}}{0.8\ r_{\text{SMA}}}\right)}{2\pi k_{\text{SMA}}L_{\text{SMA}}} \right)^{-1} \tag{7}$$

To deal with the reaction term $\Delta H_{\text{rxn}}\dot{f}_{\text{H}_2}$ in Eq. (5), we chose hydrogen (H_2) as the fuel and assumed that Eq. (8) is the only reaction path allowed. To simplify the model, we assume that the chemical reaction time scale is much smaller than the relevant heat and transport time scales [31]. As a result, the reaction happens instantaneously and proceeds to completion. In the model, O_2 is abundantly available. We used a constant heat of reaction value $\Delta H_{\text{rxn}} = 1.1996 \times 10^8$ J kg^{-1}:

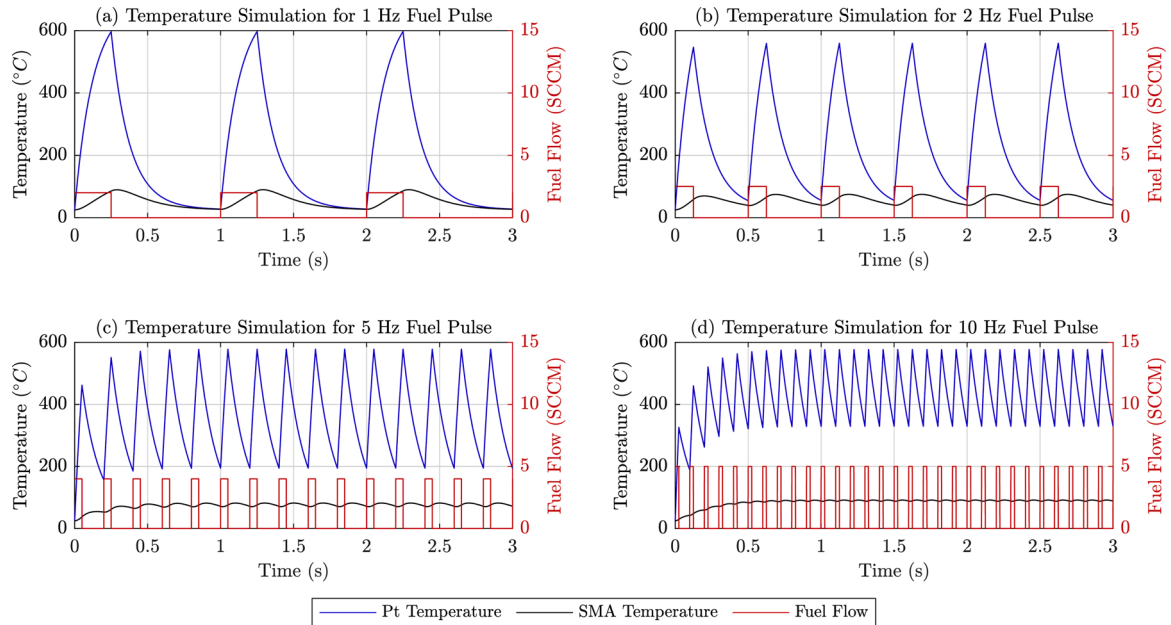$$2H_2 + O_2 \xrightarrow{\text{Pt}} 2H_2O \tag{8}$$

Fig. 6. Plots of the platinum coating layer (Pt) and the SMA wire temperatures obtained from the numerical model for a specified H_2 pulse train. In all simulations, the frequency of the fuel pulse train was specified and the duty cycle was fixed at 25%. The amplitude of the fuel pulse train was chosen to limit the maximum SMA temperature to 90 °C. As the frequency increases, there is less time available for cooling, and as a result, the steady state temperature range decreases.
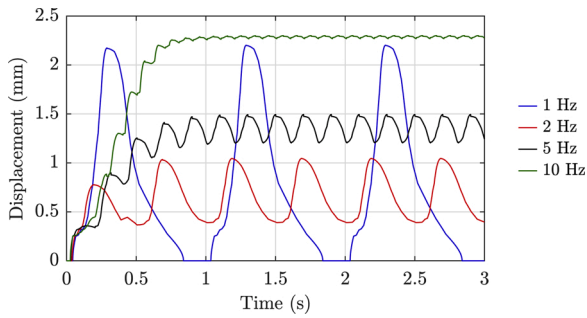
Fig. 7. Simulation results of the tip displacement for the miniature catalytic-combustion engine. The displacement range decreases as the frequency of operation increases.

Table 2
Summary of simulation predictions for the miniature catalytic-combustion engine at steady state operation for different frequencies.

f (Hz)	ΔT (°C)	Strain range (%)	Disp. (μm)
1	26–90	0.00–2.65	2202
2	40–75	0.08–0.60	656
5	70–82	0.78–1.23	304
10	85–89	2.79–2.89	42

The fuel flow rate term $\dot{f}_{H_2}(t)$ was modeled as an ideal rectangular pulse train with a duty cycle of 25% and an amplitude that varies with the pulse train frequency. The duty cycle is defined as the time fraction of the period when the fuel flow is active. The amplitude was chosen to maximize the temperature variations of the SMA for a given frequency.

The thermal model's system of coupled differential equations was solved numerically using Matlab's ode45 method. The SMA wire temperature and the coating layer temperature predicted by the model are shown in Fig. 6 for a given fuel flow rate amplitude and frequency.

To evaluate the engine's performance, we built a dynamic model of the actuator that can predict the generated tip displacement for a given temperature profile. In order to estimate the stress on the SMA wire in our actuator, we used a beam model with a tilt buckling configuration adopted from Ref. [29]. Using Eq. (9), we can solve numerically for the normal load on the SMA wires (P) for a given tip displacement (w):

$$w = b \frac{\sqrt{\frac{P}{EI}}L\left(1 - cos\sqrt{\frac{P}{EI}}L\right)}{sin\sqrt{\frac{P}{EI}}L} \tag{9}$$

In Eq. (9), L is the effective length of the actuator, taken to be 9 mm, b is the effective offset distance between the SMA wire and the beam neutral axis, and EI is the longitudinal bending stiffness of the beam. We estimated EI using lamination theory to be 10.04 μN m² [32]. The stress on the SMA can be calculated by dividing the normal load (P) by the total cross sectional area of the two sections of the SMA wire (Eq. (10)):

$$\sigma_{SMA} = \frac{P}{2A_{SMA}} \tag{10}$$

We calculated the average stress on the SMA during a cycle from the actuator's resting position ($w = 0$) to a maximum tip displacement ($w_{max} = 2$ mm) to be 145 MPa.

We then calculated the SMA strain by using the Preisach-model-based description of SMA wire dynamics described in Ref. [13]. For each frequency, we obtained the strain profile by inputting the predicted SMA temperature profiles (Fig. 6) and assuming a constant stress equal to the calculated average stress on the SMA. After, we calculated the expected tip displacement for each strain profile using Eq. (11) adopted from Ref. [29]. The obtained tip displacement (w) profiles for each frequency are shown in Fig. 7:

$$\epsilon_{SMA} = \frac{\sqrt{w^2 + L^2}}{L} - 1 \tag{11}$$

A summary of the key steady-state results from the thermal and dynamic model are shown in Table 2, where f is the frequency of the fuel flow rate pulse train, ΔT is the minimum and maximum SMA temperatures, *Strain Range* is the minimum and maximum SMA strain, and *Disp.* is the maximum one-way tip displacement of the actuator.

To increase the displacement of the catalytic actuator, we need to increase the strain range of the SMA wire. For a constant stress, the SMA wire strain behavior is correlated with its temperature [13]. As we increase the frequency of the fuel pulse train, the SMA reaches higher average temperatures and the difference between the high and low temperatures within each cycle becomes smaller. This occurs because as frequency increases, there is less time available for the SMA to reject the heat into the air. The asymmetric temperature curve of the SMA wire, where the heating phase slope is steeper than the cooling phase slope, indicates that to keep the SMA average temperature low, the cooling phase requires more time than the heating phase. Additionally, as the frequency increases, the average temperature of the coating layer increases, which slows down the heat rejection rate of the SMA wire since both layers are in direct contact. There is a significant difference between the SMA wire and the coating layer temperatures. This difference is a direct result of our choice of β in Eq. (7).

Based on the simulation results and considering its assumptions, we concluded that our proposed engine design can achieve frequencies
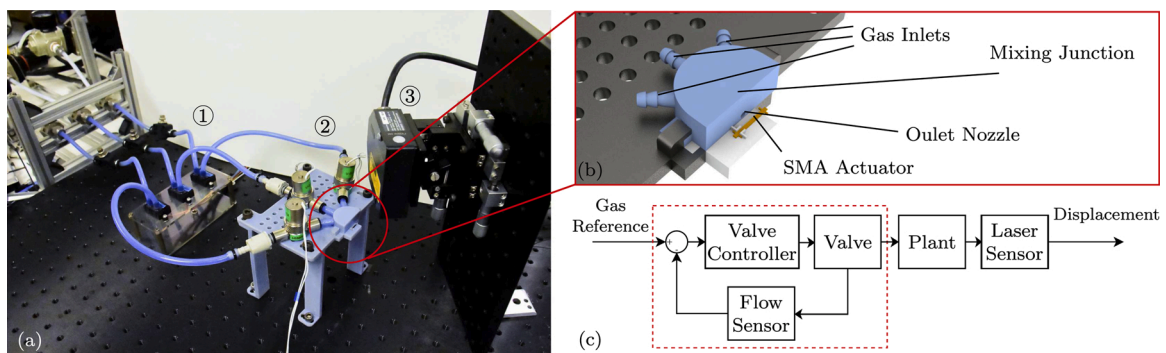

Fig. 8. Experimental characterization setup. (a.1) Gas flow sensors. (a.2) Solenoid proportional valves connected to the sensors upstream and to the mixing junction downstream. The valves are placed on a 3D printed platform. (a.3) Laser displacement sensor. (b) A close-up of the design of the 3D printed mixing junction and actuator base. The mixing junction is shown in blue. The gas flows are mixed in the junction and redirected to a nozzle that faces the actuator shown in orange. The actuator is held in place by a small piece of tape (not shown) on one end, while the other end of the actuator is free to move and perform work. (c) The closed loop feedback control scheme for the fuel delivery system is shown inside the dashed red box. The overall characterization setup utilizes the displayed open loop feedforward control scheme. (For interpretation of the references to color in this figure legend, the reader is referred to the web version of this article.)
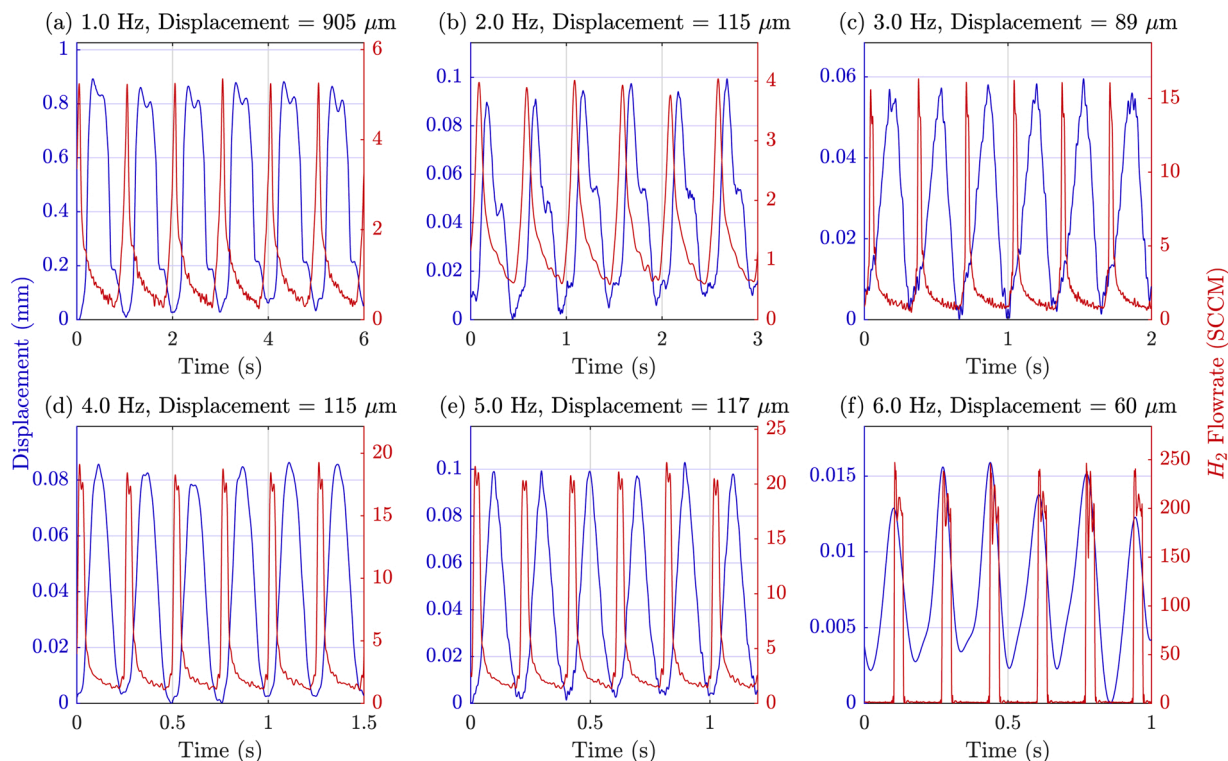
Fig. 9. Plots showing the linear displacement of the actuator tip during steady state operation for a given fuel flow rate. The actuator is displacing a 2.15 g weight against gravity.

higher than those reported in the literature for SMA-based miniature catalytic-combustion engines. Furthermore, the dynamic model predicts large tip displacements associated with the high operational frequencies. From the simulations, we see that it is possible to have large differences between the average temperatures of the SMA wire and the coating layer by controlling the heat transfer coefficient $(UA)_{SMA-Pt}$. This can be achieved through insulation and through decreasing the layers' contact area. Allowing the temperature of the SMA and the coating layer to differ widely enables more flexibility regarding the choice of fuel. Furthermore, it is evident from the simulation that a precise fuel mechanism is needed to deliver fuel in high frequency pulses. Imperfections in the fuel delivery system and diffusion effects will diffuse the fuel pulses, decrease the temperature range, and decrease the maximum displacement for a given frequency. By narrowing the width of the fuel pulses, there is more time available for cooling. The simulation indicates that cooling is the limiting factor at higher frequencies. Thus, to achieve higher frequencies, strategies such as active cooling must be employed.

4. Experiment setup

We built an experiment setup to characterize the performance of the catalytic-combustion miniature engine and test different control strategies. We aimed to design a system that can characterize the behavior of different miniature catalytic-combustion SMA engines using different gaseous fuels and different mixing ratios with air and N_2. To achieve this goal, we built the system shown in Fig. 8.

We place the actuator in the base shown in Fig. 8b, where one end is fixed to the base while the other end is free. The gas flow out of the nozzle is a mixture of fuel, air, and N_2. The flow rates and mixing ratios are controlled by the fuel delivery system. The closed loop feedback control scheme of the fuel delivery system and the open loop feedforward control scheme of the overall setup are shown in Fig. 8c. We set a reference signal for the gas flow rates and thus control the temperature of the SMA which determines the actuator displacement.

To obtain high frequency actuation we need a fast and precise fuel delivery system. To achieve this goal, we utilized a custom-built fast-response high-precision fuel delivery apparatus, which consists of three air-flow sensors, three solenoid-proportional valves (Kelly Pneumatics, KPI-VP20-09025-V), pressure regulators, and a 3D printed mixing junction. For the H_2 and air gasses, we used 200 SCCM air-flow sensors (Honeywell, HAFBLF0200CAAX5). For the N_2 gas, we used a 750 SCCM air-flow sensor (Honeywell, HAFBLF0750CAAX5). A pressure regulator was installed upstream of the flow sensors to set the maximum gas pressure allowed in the system. The different components of the fuel delivery apparatus were connected using $1/4''$ tubing. The mixing juncture was 3D printed using Objet30 Pro (Stratasys) and *VeroBlue* printing material. The junction was designed to minimize the distance between the valve outlet and the SMA wire in order to minimize the diffusion of fuel pulses.

To design the valve controller shown in Fig. 8c, we performed a system identification process and designed an LTI controller using the methods detailed in Ref. [33,34]. The response time of the fuel delivery system to a step input when using N_2 gas is 30 ms. The flow delivery system we built is significantly faster than commercial controlled flow actuators, which have a response time in the order of seconds.

To characterize the actuation behavior, we use a displacement laser sensor (keyence, LK-G3001 and LK-G32). The sensor measures the linear displacement component of the free tip of the actuator with a 0.05 μm accuracy. The experimental setup does not directly measure the SMA wire temperature. For thin SMA wires like the ones used in this design, most commercially available thin thermocouples are not suitable to measure the temperature because their diameters are similar to those of the SMA wires and thus cannot produce unintrusive measurements. Furthermore, thin thermocouples ($r = 50$ μm) have a maximum bandwidth of 1 Hz and as a result cannot measure faster temperature signals [35].

All data acquisition, signal processing, and real-time control tasks are performed using a Mathworks xPC-Target5.5 system and a PCI-6229 National Instruments AD/DA board running at the sample-and-hold
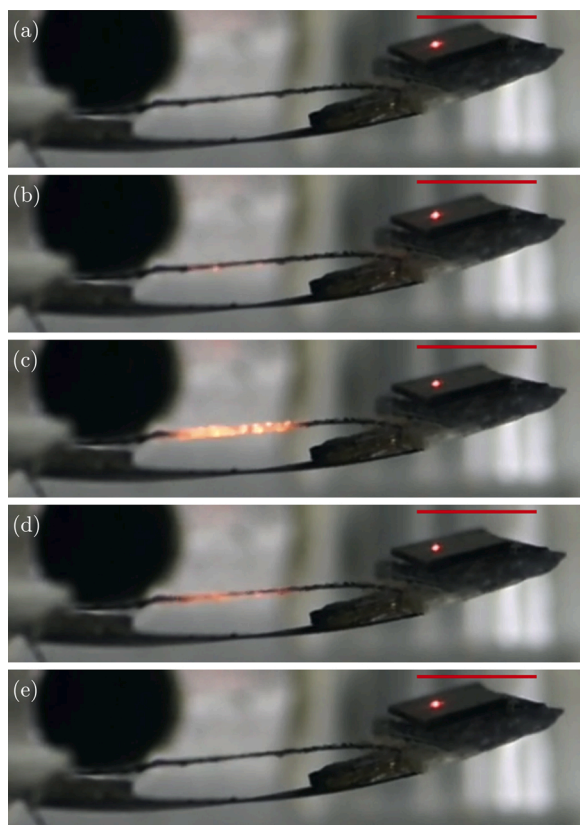
Fig. 10. Frames from a video showing a full operational cycle of the catalytic actuator. The time between frames (a) and (e) is 1 s. A red vertical line was added in the same position in all frames to make the displacement of the actuator tip clearer. The red dot on the actuator tip is the reflection of the displacement laser sensor. (a) The actuator is hot and fully contracted. This is the beginning of the cooling phase. (b) As the actuator cools down by convective and conductive forces it starts to expand, returning the actuator to its resting position. At this point, the fuel gas reaches the catalytic layer and starts reacting. This can be deducted from the slightly red glow appearing on the catalyst's surface. (c) The actuator fully reaches the relaxed position and the catalytic combustion reaction is at its maximum rate. This is evident by the red glow seen on the catalytic layer. (d) As the heat transfers from the catalytic layer to the SMA wire and increases its temperature, the actuator starts to bend. Some fuel gas is still reacting on the catalyst surface. (e) The SMA temperature is at its maximum and the actuator is fully bent and is at the beginning of the actuation cycle again. (For interpretation of the references to color in this figure legend, the reader is referred to the web version of this article.)

rate of 1 kHz.

The H_2 reference signal was set as a pulse train with a specified frequency and a duty cycle of 25%, similar to the fuel signal shown in Fig. 6. The air flow rate was chosen to achieve a stoichiometric mixture when the H_2 flow was active (the heating phase). When the H_2 flow was inactive (the cooling phase), we increased the air flow rate. Our goal of ramping up the air flow rate during the cooling phase is to increase the convective cooling rate. The air flow rate during the cooling phase was chosen using trial and error to get the highest frequency and displacement results within the limits of the fuel delivery system. The N_2 flow was set at a constant value for each frequency. The purpose of the N_2 gas was to decrease the overall temperature of the reaction without changing the combustion equivalence ratio during the heating phase and to help with the convective cooling during the cooling phase.

We attached a weight to the actuator's free tip to demonstrate the engine's ability to perform work. In each experiment, we started with a small fuel flow rate and slowly increased it. It usually takes the system 1–10 s to reach steady state. After steady state was reached, we increased the fuel rate again. This process was repeated until a

satisfactory displacement was observed.

5. Characterization results and discussion

We performed a set of experiments to investigate the engine performance while operating at different frequencies. In Fig. 9, we show a summary of the engine characterization results for 1–6 Hz. The maximum one way displacement achieved at each frequency is calculated and displayed in the titles of Fig. 9. Each figure shows the displacement and H_2 flow rate as functions of time for 6 steady state cycles. We only display the steady state portion of the operation for clarity. For each frequency test shown, we attached a 2.15 g weight to the free tip of the actuator. As a result, the actuator is performing useful work during each cycle. The maximum displacement achieved by the actuator is 0.9 mm when operated at 1 Hz. We expect that the maximum displacement occurs when operating at the lowest frequency because as the frequency increases, the time available for cooling decreases, which increases the overall average temperature. There is a delay between the measured fuel flow rate signal and the displacement signal. This delay is caused by the physical distance between the valve opening and the Pt coating layer. It is also caused by the time it takes for the heat to transfer between the Pt coating and the SMA wire. The actuator shows significant displacements at all frequencies. The smallest displacement occurred when operating the actuator at 6 Hz (60 μm).

We video recorded the actuator during all of its operational cycles. By analyzing the videos, we can verify the displacement results and learn more about the processes taking place during the actuation cycle. In Fig. 10, a full cycle for the actuator is shown during operation at 1 Hz frequency with no attached weights. The time between frames (a) and (e) is 1 s. The combustion process taking place on the Pt catalyst surface can be visually observed through the red glow produced by the released heat of reaction.

The visual observations in Fig. 10 validate our assumption in the numerical model that it is possible, by controlling β, to have the catalyst average temperature be significantly higher than the SMA wire average temperature. This can be observed by noticing the glowing red color of the Pt catalyst which indicates an approximate minimum temperature of 525 °C [36]. We also know that the SMA temperature must be below 150 °C, because above that temperature the SMA is outside of its hysteresis loop and does not significantly strain in response to temperature changes [13]. Thus, by controlling the heat transfer rate between the SMA wire and the coating layer we can decouple their temperatures. The decoupling allows us to use different chemical fuels than hydrogen, such as propane and butane, more easily. Those fuels require higher ignition temperatures for the catalytic combustion to take place [37]. The advantage of those fuels over hydrogen is their ease of storage and handling. The decoupling acts as a low pass filter, where large oscillations in the Pt temperature lead to small oscillations in the SMA temperature. With appropriate tuning, the Pt can be adequately hot for the fuel to react on its surface, while the SMA is still within its operating shape-memory effect temperatures.

We performed another set of experiments to determine the maximum work output of the engine. In Fig. 11, we show frames from a video of the actuator lifting a 4.55 g mass. The snapshot provides visual evidence of the useful work the actuator can perform. We operated the engine with different attached weights and measures the upward displacement generated by the engine. Then, we calculated the engine work output using Eq. (12):

$$W_{\text{Engine}} = \text{Fd} = mgd \qquad (12)$$

where m is the mass of the attached weight. We measured the maximum average work output of the engine to be 39.5 μJ at 1 Hz, corresponding to 39.5 μW of average power. This output takes place when the attached weight is 4.55 g and for an average displacement of 0.88 mm. This result demonstrates the ability of the actuator to lift a mass 650 times its
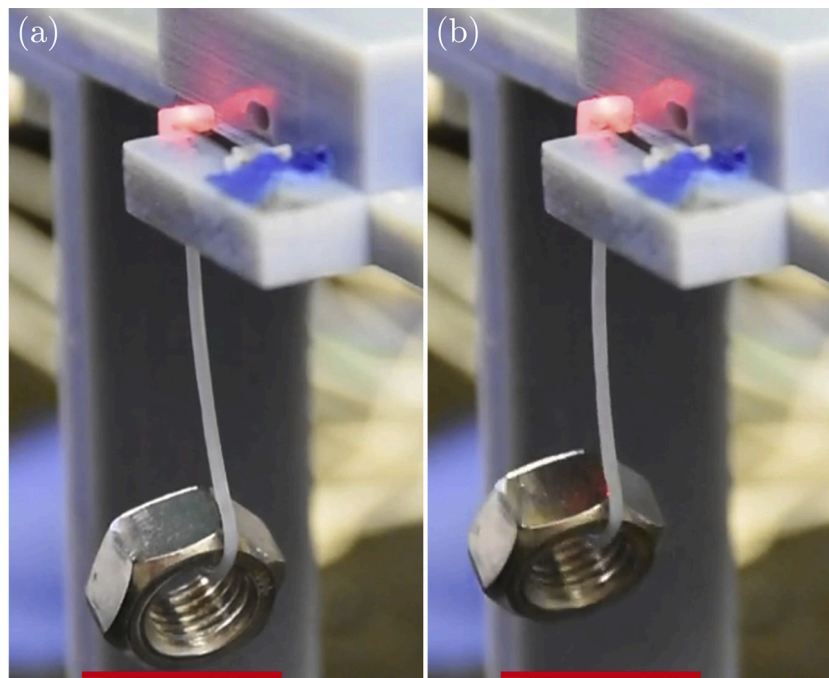
Fig. 11. Frames from a video showing the actuator lifting a 4.55 g mass 0.91 mm at a frequency of 1 Hz. A red line is added to signify the movement of the weight. (a) The actuator is in its resting position. (b) The actuator is fully bent achieving its maximum displacement and 39.5 μJ of work. (For interpretation of the references to color in this figure legend, the reader is referred to the web version of this article.)

weight utilizing catalytic combustion, corresponding to a specific power of 5.65 W kg^{-1} when not accounting for the fuel storage and delivery system weights.

Using the calculated engine work output, we can compute a thermal efficiency of our proposed miniature engine using the definition in Eq. (13):

$$\eta = \frac{W_{\text{Engine}}}{\text{FuelEnergyInput}} \times 100 \tag{13}$$

The fuel energy input is calculated by multiplying the total fuel input during a cycle by the heat of reaction of H$_2$ (ΔH_{rxn}). The formula in Eq. (13) does not take into account the energy needed to operate the fuel delivery system. The engine thermal efficiency for the maximum average work output case was calculated to be 0.02%. The current engine design was not optimized to have high efficiency. We suspect that the low efficiency occurs because most of the fuel added into the system does not come into contact with the Pt layer and thus does not contribute to heating up the SMA. To increase the thermal efficiency, we need a more targeted fuel delivery design that decreases the amount of unreacted fuel.

The visual observations (Figs. 10 and 11) combined with the displacement results (Fig. 9) confirm the simulation prediction that higher frequencies can be achieved in miniature catalytic-combustion SMA engines. By utilizing active cooling, we can shorten the time needed to cool down the SMA to an acceptable level to achieve significant displacement at rates up to 6 Hz. We can achieve those frequencies by ensuring the fuel pulses are delivered precisely and quickly. By decreasing the heat transfer rate between the catalytic coating layer and the SMA wire we can decouple their temperatures, allowing us more operational freedom and flexibility in terms of fuel choice.

While the simulations predicts that we can operate the actuator at 10 Hz and still observe temperature and displacement variations, we were not able to achieve frequencies higher than 6 Hz using the current actuator and characterization setup. Furthermore, the observed experimental displacements were smaller than the model's predicted displacements. The discrepancy between the model and the experiment is caused by the simulation's assumption of instant fuel delivery. In the experiment, we control and measure the fuel mixture flow rate at the gas valves. The mixture that reaches that catalytic layer differs from what we measured because of the diffusion processes that take place in the path between the valves and the Pt coating. Compared with the rectangular shaped fuel pulses simulated in Fig. 6 and measured in Fig. 9, the catalytic layer most likely experiences sinusoidal-like fuel pulses with a duty cycle larger than 25%. The diffusion of the fuel pulses increases the duration of the heating phase which does not allow for enough cooling to take place.

Additionally, the current setup is limited by the maximum speed of the valve system. To increase the actuation frequency, we need to send narrower gas pulses in order to keep the same duty cycle that allows for sufficient cooling time. Narrower fuel pulses will allow higher frequencies comparable to those reported in the literature for electrically heated SMA actuators [16,21]. However, the fuel pulse width cannot be smaller than approximately two times the response time of the fuel delivery system. In the current setup, we estimate the minimum pulse width that we can use to be 50 μs. For comparison, if we operate the actuator at 10 Hz and require a duty cycle of 25%, the fuel pulse width must be 25 μs.

6. Conclusions

We presented and tested a new design for a 7 mg miniature catalytic-combustion SMA engine that can be used for millimeter-scale robotic actuation. The innovate engine design was made possible by using thin SMA wires combined with smart material composites. We performed thermal and dynamic modeling to predict the maximum possible operating frequencies and associated displacements. The miniature engine was then tested on a versatile characterization setup that can test different control strategies. To maximize the actuation frequency, we built a custom-built fast-response high-precision delivery system. The miniature engine was demonstrated to work effectively in an operational frequency range of 1–6 Hz. The engine can deliver 39.5 μJ of work at a rate of 1 Hz.

The proposed miniature engine design can serve as a building block for autonomous microrobotic applications that aim to provide onboard power using chemical fuels. The characterization setup we built can be used to test control and fuel delivery strategies. Then, a pre-programmed, onboard tank and valve system can deliver the fuel to the actuator in a way that achieves the desired functional and performative requirements of the microrobots.

Funding

Conflict of interest

None declared.

Appendix A. Supplementary data

Supplementary data associated with this article can be found, in the online version, at https://doi.org/10.1016/j.sna.2021.112818.

References

[1] J.M. Beer, A.D. Fisk, W.A. Rogers, Toward a framework for levels of robot autonomy in human-robot interaction, J. Human-Robot Interact. 3 (2014) 74.
[2] M.-S. Kim, H.-T. Lee, S.-H. Ahn, Laser controlled 65 micrometer long microrobot made of ni-ti shape memory alloy, Adv. Mater. Technol. 4 (2019) 1900583.
[3] S. Hollar, A. Flynn, C. Bellew, K. Pister, Solar powered 10 mg silicon robot, The Sixteenth Annual International Conference on Micro Electro Mechanical Systems, MEMS-03 Kyoto (2003) 706–711.
[4] T. Yasuda, I. Shimoyama, H. Miura, Microrobot actuated by a vibration energy field, Sens. Actuators A: Phys. 43 (1994) 366–370.
[5] K. Vollmers, D.R. Frutiger, B.E. Kratochvil, B.J. Nelson, Wireless resonant magnetic microactuator for untethered mobile microrobots, Appl. Phys. Lett. 92 (2008) 144103.
[6] C. Pawashe, S. Floyd, M. Sitti, Modeling and experimental characterization of an untethered magnetic micro-robot, Int. J. Robot. Res. 28 (2009) 1077–1094.
[7] D. Lee, S. Kim, Y.-L. Park, R.J. Wood, Design of centimeter-scale inchworm robots with bidirectional claws, 2011 IEEE International Conference on Robotics and Automation (2011) 3197–3204.
[8] B. Goldberg, R. Zufferey, N. Doshi, E.F. Helbling, G. Whittredge, M. Kovac, R. J. Wood, Power and control autonomy for high-speed locomotion with an insect-scale legged robot, IEEE Robot. Autom. Lett. 3 (2018) 987–993.
[9] D.S. Contreras, D.S. Drew, K.S. Pister, First steps of a millimeter-scale walking silicon robot, 2017 19th International Conference on Solid-State Sensors, Actuators and Microsystems (TRANSDUCERS) (2017) 910–913.
[10] B. Kim, M.G. Lee, Y.P. Lee, Y. Kim, G. Lee, An earthworm-like micro robot using shape memory alloy actuator, Sens. Actuators A: Phys. 125 (2006) 429–437.
[11] A.M. Hoover, E. Steltz, R.S. Fearing, Roach: An autonomous 2. 4 g crawling hexapod robot, 2008 IEEE/RSJ International Conference on Intelligent Robots and Systems (2008) 26–33.
[12] J.-M. Breguet, S. Johansson, W. Driesen, U. Simu, A review on actuation principles for few cubic millimeter sized mobile micro-robots, Proceedings of the 10th International Conference on New Actuators (Actuator 2006), CONF (2006) 74–381.
[13] Z.G. Joey, L. Chang, N.O. Pérez-Arancibia, Position control of a shape-memory alloy actuator using a Preisach-model-based inverse-temperature method, 2019 American Control Conference (ACC) (2019) 3801–3808.
[14] D.J. Hartl, D.C. Lagoudas, Aerospace applications of shape memory alloys, Proc. Inst. Mech. Engrs. Part G J. Aerosp. Eng. 221 (2007) 535–552.
[15] X. Ji, X. Liu, V. Cacucciolo, M. Imboden, Y. Civet, A. El Haitami, S. Cantin, Y. Perriard, H. Shea, An autonomous untethered fast soft robotic insect driven by low-voltage dielectric elastomer actuators, Sci. Robot. 4 (2019).
[16] X.-T. Nguyen, A.A. Calderón, A. Rigo, Z.G. Joey, N.O. Pérez-Arancibia, Smallbug: A 30-mg crawling robot driven by a high-frequency flexible sma microactuator, IEEE Robot. Autom. Lett. 5 (2020) 6796–6803.
[17] G. Zubi, R. Dufo-López, M. Carvalho, G. Pasaoglu, The lithium-ion battery: state of the art and future perspectives, Renew. Sustain. Energy Rev. 89 (2018) 292–308.
[18] L. Ricotti, B. Trimmer, A.W. Feinberg, R. Raman, K.K. Parker, R. Bashir, M. Sitti, S. Martel, P. Dario, A. Menciassi, Biohybrid actuators for robotics: a review of devices actuated by living cells, Sci. Robot. 2 (2017).
[19] A. Johnson, J. Kramer, State-of-the-art of shape memory actuators, in: 6th International Conference on New Actuators, Bremen, Germany, 1998.
[20] X. Yang, L. Chang, N.O. Pérez-Arancibia, An 88-milligram insect-scale autonomous crawling robot driven by a catalytic artificial muscle, Sci. Robot. 5 (2020).
[21] Z. Wang, G. Hang, J. Li, Y. Wang, K. Xiao, A micro-robot fish with embedded sma wire actuated flexible biomimetic fin, Sens. Actuators A: Phys. 144 (2008) 354–360.
[22] S.R. Kirkpatirck, A. Siahmakoun, T.M. Adams, Z. Wang, Shape memory alloy mems heat engine, US Patent 7,444,812 (2008).
[23] D. Avirovik, R.A. Kishore, D. Vuckovic, S. Priya, Miniature shape memory alloy heat engine for powering wireless sensor nodes, Energy Harvest. Syst. 1 (2014) 13–18.
[24] H. Aono, R. Imamura, O. Fuchiwaki, Y. Yamanashi, K.F. Böhringer, Formulation and optimization of pulley-gear-type sma heat engine toward microfluidic mems motor, in: 2014 IEEE/RSJ International Conference on Intelligent Robots and Systems, IEEE, 2014, pp. 2839–2845.
[25] V.H. Ebron, Z. Yang, D.J. Seyer, M.E. Kozlov, J. Oh, H. Xie, J. Razal, L.J. Hall, J. P. Ferraris, A.G. MacDiarmid, et al., Fuel-powered artificial muscles, Science 311 (2006) 1580–1583.
[26] Y. Tadesse, A. Villanueva, C. Haines, D. Novitski, R. Baughman, S. Priya, Hydrogen-fuel-powered bell segments of biomimetic jellyfish, Smart Mater. Struct. 21 (2012) 045013.
[27] M. Wehner, R.L. Truby, D.J. Fitzgerald, B. Mosadegh, G.M. Whitesides, J.A. Lewis, R.J. Wood, Nature 536 (2016) 451–455.
[28] Y. Shi, J. Whalen, P. Ronney, Hydrocarbon ignition on high surface area pt-electroplated wires, AIAA Scitech 2019 Forum (2019) 2370.
[29] Z. Chaudhry, C.A. Rogers, Bending and shape control of beams using sma actuators, J. Intell. Mater. Syst. Struct. 2 (1991) 581–602.
[30] G. Nellis, S.A. Klein, Heat Transfer, Cambridge University Press, 2012.
[31] C. Spadaccini, J. Peck, I. Waitz, Catalytic Combustion Systems for Microscale Gas Turbine Engines, 2007.
[32] J.N. Reddy, Mechanics of Laminated Composite Plates and Shells: Theory and Analysis, CRC press, 2003.
[33] N. Arancibia, S. Gibson, T.-C. Tsao, et al., Adaptive control of mems mirrors for beam steering, ASME 2004 International Mechanical Engineering Congress and Exposition, American Society of Mechanical Engineers Digital Collection (2004) 71–80.
[34] Y.-L. Park, B.-r. Chen, N.O. Pérez-Arancibia, D. Young, L. Stirling, R.J. Wood, E. C. Goldfield, R. Nagpal, Design and control of a bio-inspired soft wearable robotic device for ankle-foot rehabilitation, Bioinsp. Biomimetics 9 (2014) 016007.
[35] K. Farahmand, J.W. Kaufman, Experimental measurement of fine thermocouple response time in air, Exp. Heat Transfer 14 (2001) 107–118.
[36] J.W. Draper, On the production of light by heat, J. Franklin Inst. 44 (1847) 122–128.
[37] P. Cho, C.K. Law, Catalytic ignition of fuel/oxygen/nitrogen mixtures over platinum, Combust. Flame 66 (1986) 159–170.

Fares Maimani completed his bachelor's degree in Chemical Engineering at the University of California, Berkeley and his master's degree in Mechanical Engineering at King Abdullah University of Science and Technology (KAUST). He is currently pursuing his Ph. D. at the Department of Aerospace and Mechanical Engineering, University of Southern California (USC).

Dr. Ariel A. Calderón completed his bachelor's degree in Mechanical Engineering at Universidad de Chile and his master's and Ph.D. degrees in Mechanical Engineering at the Department of Aerospace and Mechanical Engineering, University of Southern California (USC). He is currently a Postdoctoral Associate at University of California, Los Angeles.

Dr. Xiufeng Yang completed his bachelor's degree in Mechanical Engineering at Huazhong University of Science and Technology and his master's and PhD degrees in Mechanical Engineering at the Department of Aerospace and Mechanical Engineering, University of Southern California (USC). He is currently an engineer Applied Materials.

Alberto Rigo completed his bachelor's and master's degrees in Aerospace Engineering at Politecnico di Milano. He is currently pursuing his Ph.D. at the Department of Aerospace and Mechanical Engineering, University of Southern California (USC).

Dr. Joey Z. Ge completed his bachelor's degree in Mechanical Engineering at Columbia University and his master's and Ph.D. degrees in Mechanical Engineering at the Department of Aerospace and Mechanical Engineering, University of Southern California (USC). He is currently an engineer Applied Materials.

Néstor O. Pérez-Arancibia received the Ph.D. degree in mechanical engineering from the University of California, Los Angeles (UCLA) in 2007. From October 2007 to March 2010, he was a Postdoctoral Scholar in the Mechanical and Aerospace Engineering Department at UCLA. From April 2010 to March 2013, he was a Postdoctoral Fellow, and from April 2013 to August 2013, he was a Research Associate with the Microrobotics Laboratory and the Wyss Institute at Harvard University. Since August 2013, he has been at the University of Southern California (USC), where he founded and directs the Autonomous Microrobotic Systems Laboratory (AMSL).